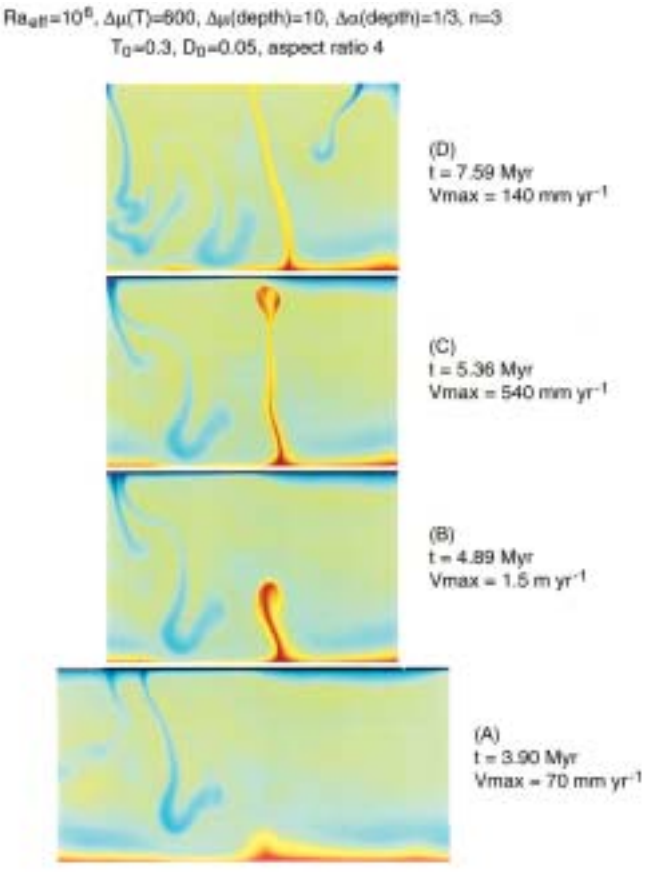

Figure 9.23. Snapshots of temperature showing development of a localized high-velocity upwelling in two-dimensional thermal convection with temperature- and stress-dependent viscosity, from calculations by Larsen and Yuen (1997a). Time increases from bottom to top at approximately 1 Myr intervals. Peak fluid velocities are 0.7, 1.5, 0.54, and 0.14 m yr^{-1}, respectively.

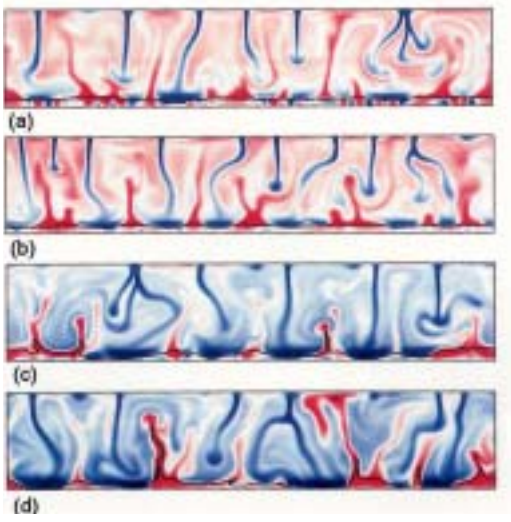

Figure 9.29. Snapshots of residual temperatures (relative to the horizontally averaged temperature) in two-dimensional, thermochemical convection with an initial dense basal layer. The thin solid line is the boundary between extra dense material and background material. (a) κ is constant and $B = 1$, (b) κ is increased by a factor of 2 in the extra dense material and $B = 1$, (c) κ is constant and $B = 0.6$, (d) κ is increased by a factor of 2 in the extra dense material and $B = 0.6$. After Montague et al. (1998).

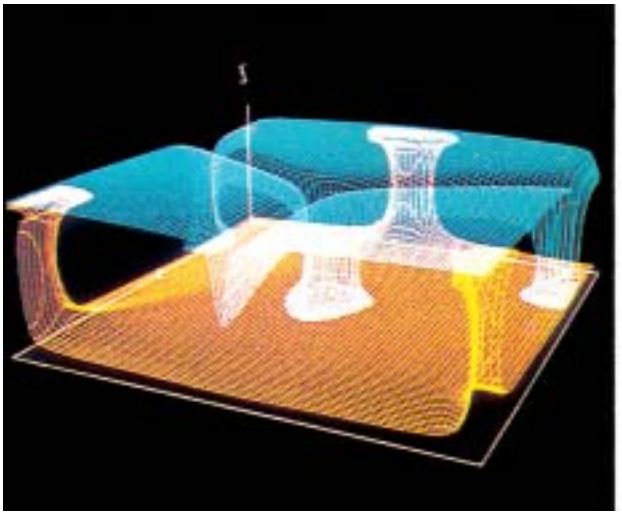

Figure 10.15. Constant temperature surfaces (dimensionless temperatures 0.25 and 0.75) in steady hexagonal cell convection at $Ra = 10^5$ in a bottom- heated rectangular box with dimensions $3 \times 3 \times 1$ (normalized by depth). After Travis et al. (1990a).

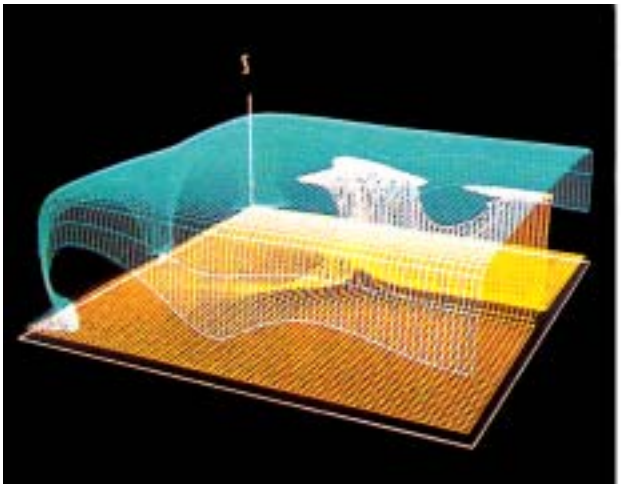

Figure 10.17. Constant temperature surfaces (dimensionless temperatures 0.25 and 0.75) in steady three-dimensional rectangular cell convection in a $3 \times 3 \times 1$ rectangular box heated from below at $Ra = 10^5$. After Travis et al. (1990a).

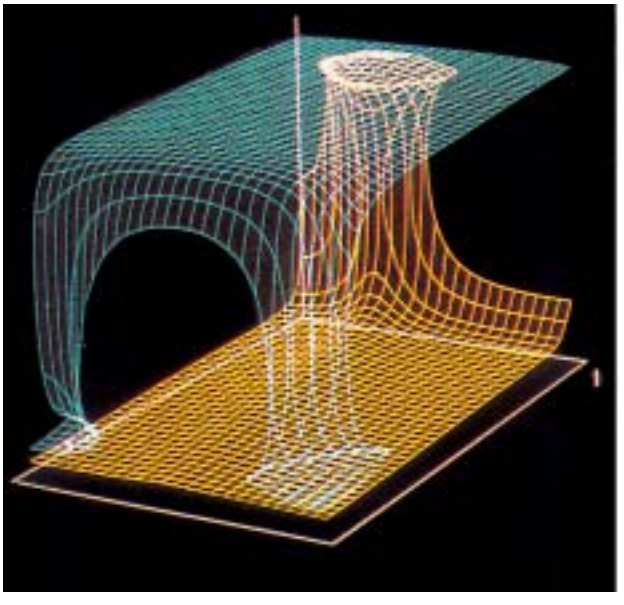

Figure 10.19. Isothermal surfaces (dimensionless temperatures 0.25 and 0.75) in three-dimensional bimodal convection in a bottom-heated rectangular box ($1.7 \times 1 \times 1$) at $Ra = 10^5$. The depth of the box is unity. After Travis et al. (1990a).

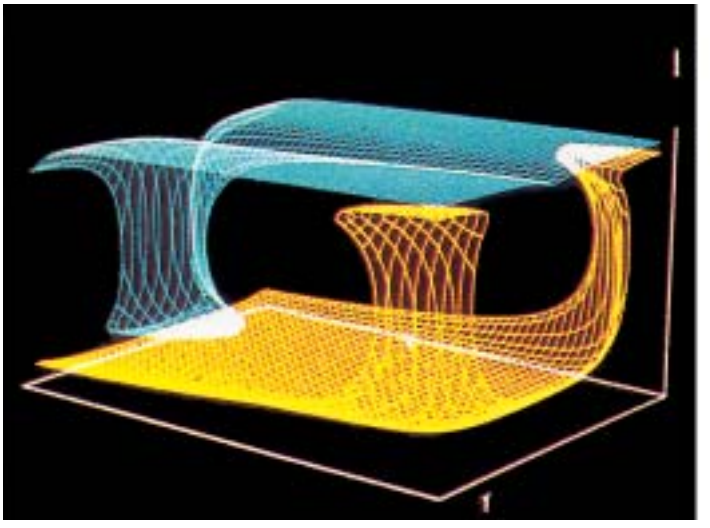

Figure 10.21. Isothermal surfaces (dimensionless temperatures 0.25 and 0.75) in steady bimodal convection in a bottom-heated rectangular box ($1.96 \times 1.41 \times 1$) at $Ra = 4 \times 10^4$. The depth of the box is unity. After Travis et al. (1990a).

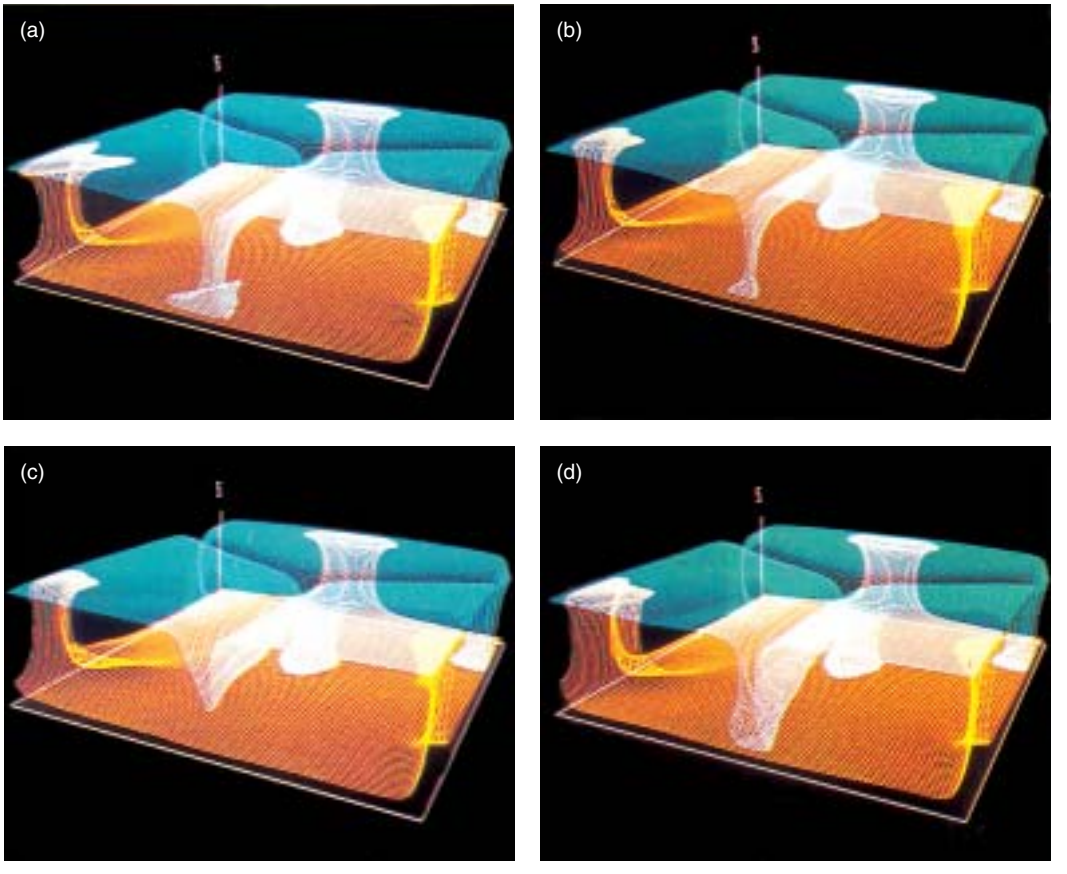

Figure 10.26. Unsteady hexagonal convection in a $3.5 \times 3.5 \times 1$ rectangular box with stress-free boundaries heated from below at $Ra = 10^5$. Isothermal surfaces (dimensionless temperatures 0.25 and 0.75) are shown at dimensionless times (a) $t = 0.5260$, (b) $t = 0.5277$, (c) $t = 0.5294$, and (d) $t = 0.5311$ during one cycle of a variable downflow plume. After Travis et al. (1990a).

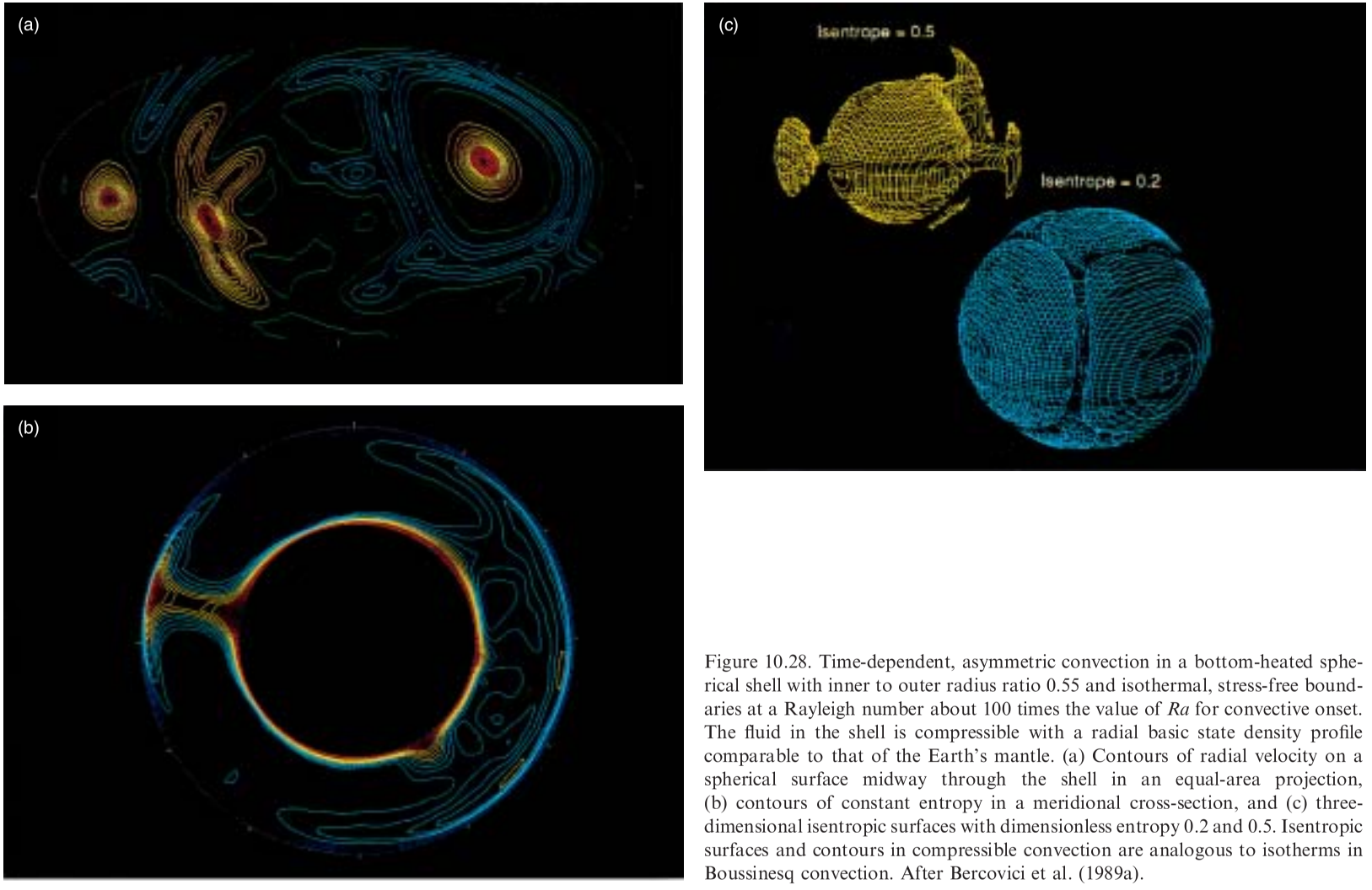

Figure 10.28. Time-dependent, asymmetric convection in a bottom-heated spherical shell with inner to outer radius ratio 0.55 and isothermal, stress-free boundaries at a Rayleigh number about 100 times the value of Ra for convective onset. The fluid in the shell is compressible with a radial basic state density profile comparable to that of the Earth's mantle. (a) Contours of radial velocity on a spherical surface midway through the shell in an equal-area projection, (b) contours of constant entropy in a meridional cross-section, and (c) three-dimensional isentropic surfaces with dimensionless entropy 0.2 and 0.5. Isentropic surfaces and contours in compressible convection are analogous to isotherms in Boussinesq convection. After Bercovici et al. (1989a).

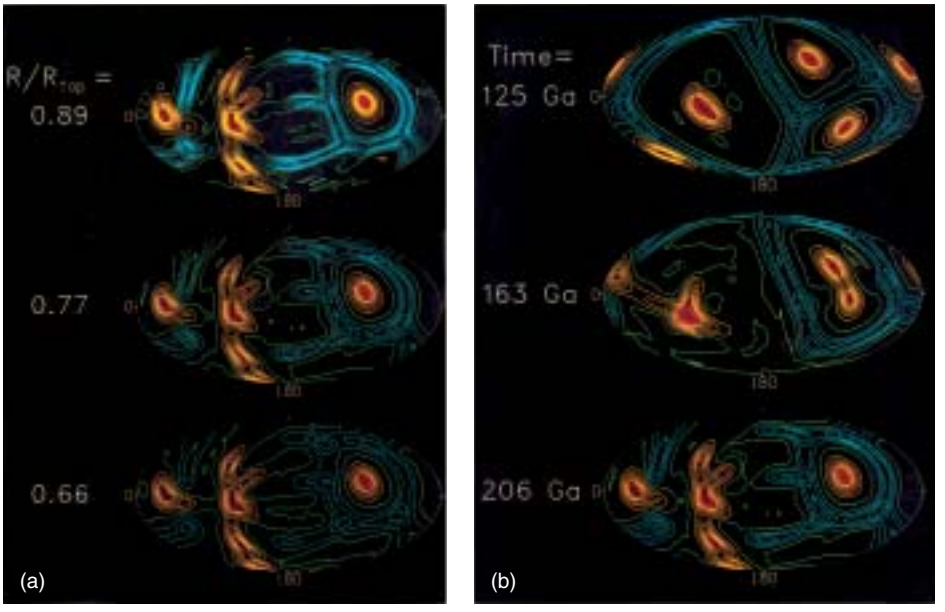

Figure 10.29. Contours of radial velocity in the calculation of Figure 10.28 for different depths at a given instant of time (a) and for different times at one depth (midway through the shell). (b) After Bercovici et al. (1989c).

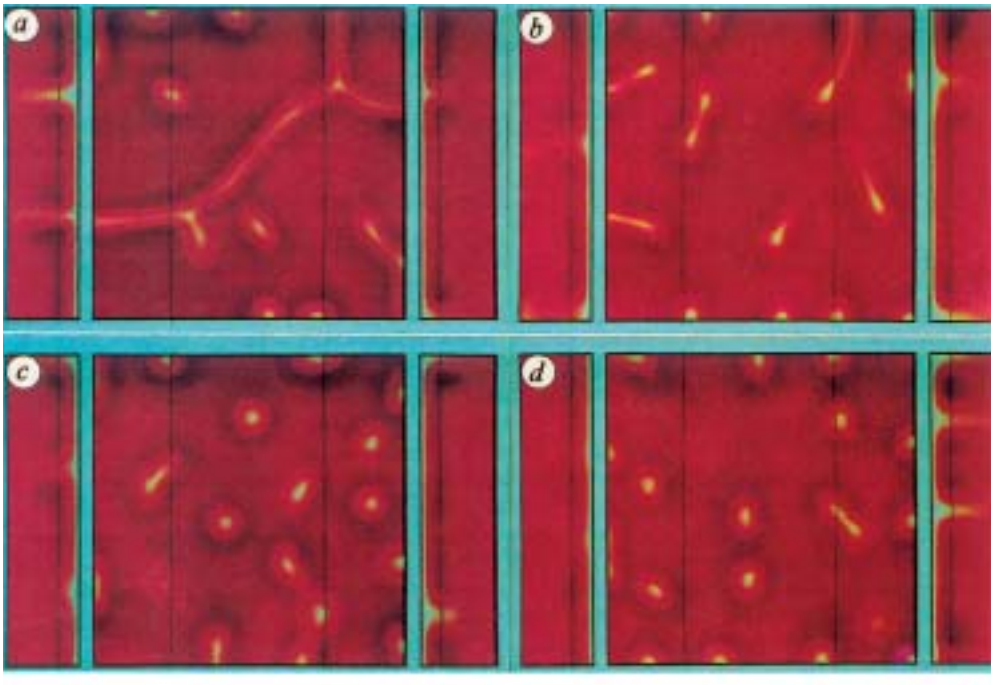

Figure 10.30. Temperature variations due to convection in a $4 \times 4 \times 1$ internally heated rectangular box of constant viscosity Boussinesq fluid. The upper and lower boundaries are stress free and the bottom surface is insulated. Color indicates temperatures: the average temperature of the box is red, grading to white for colder fluid and black for hotter fluid. The square horizontal section in the middle is at a depth of 0.25 and the vertical sections to either side are 0.25 from opposite sides of the box (up is inward for the vertical sections). The different panels correspond to different dimensionless times: (a) 0.0911, (b) 0.1327, (c) 0.1630, and (d) 0.1945. After Houseman (1988).

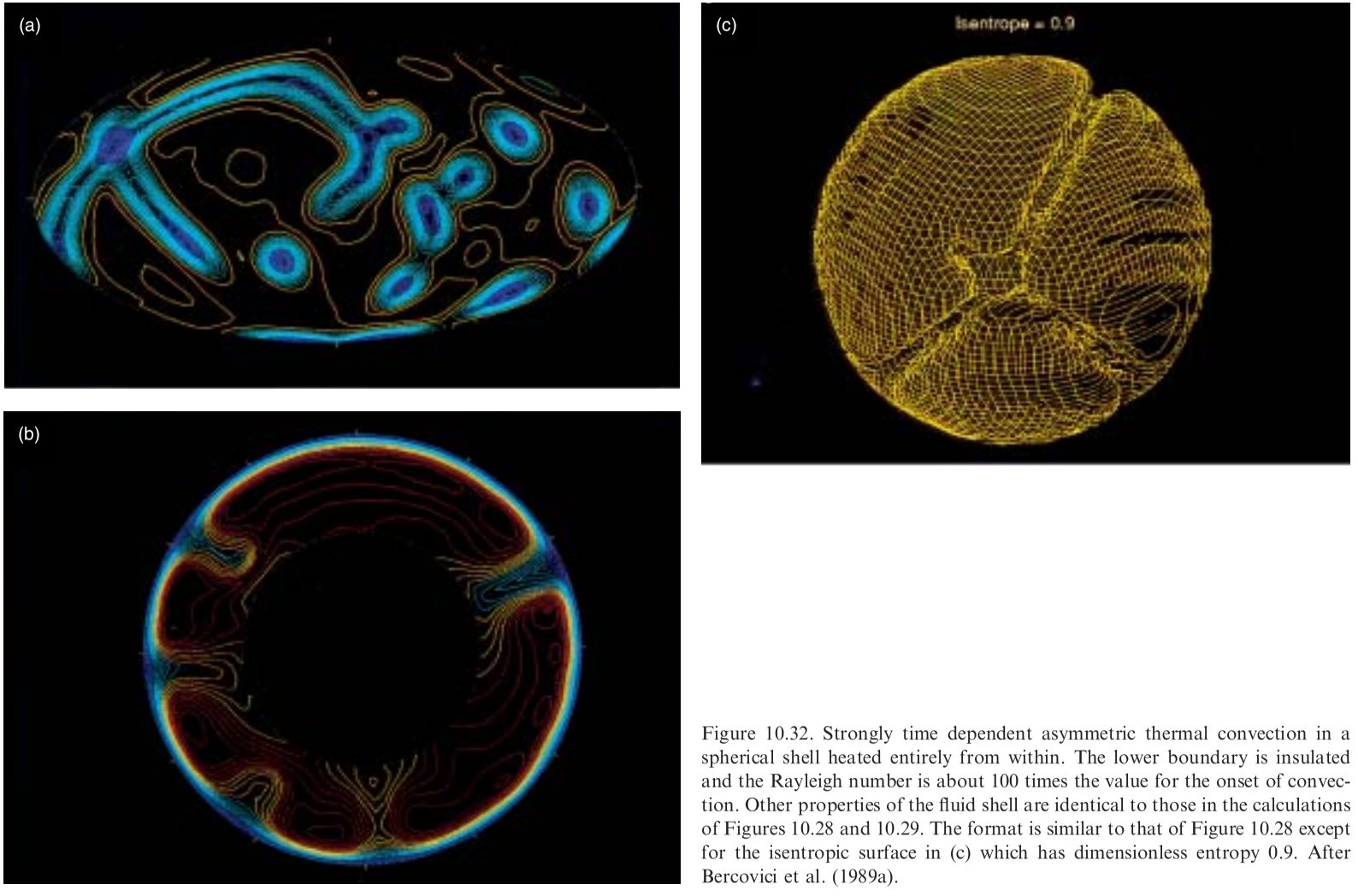

Figure 10.32. Strongly time dependent asymmetric thermal convection in a spherical shell heated entirely from within. The lower boundary is insulated and the Rayleigh number is about 100 times the value for the onset of convection. Other properties of the fluid shell are identical to those in the calculations of Figures 10.28 and 10.29. The format is similar to that of Figure 10.28 except for the isentropic surface in (c) which has dimensionless entropy 0.9. After Bercovici et al. (1989a).

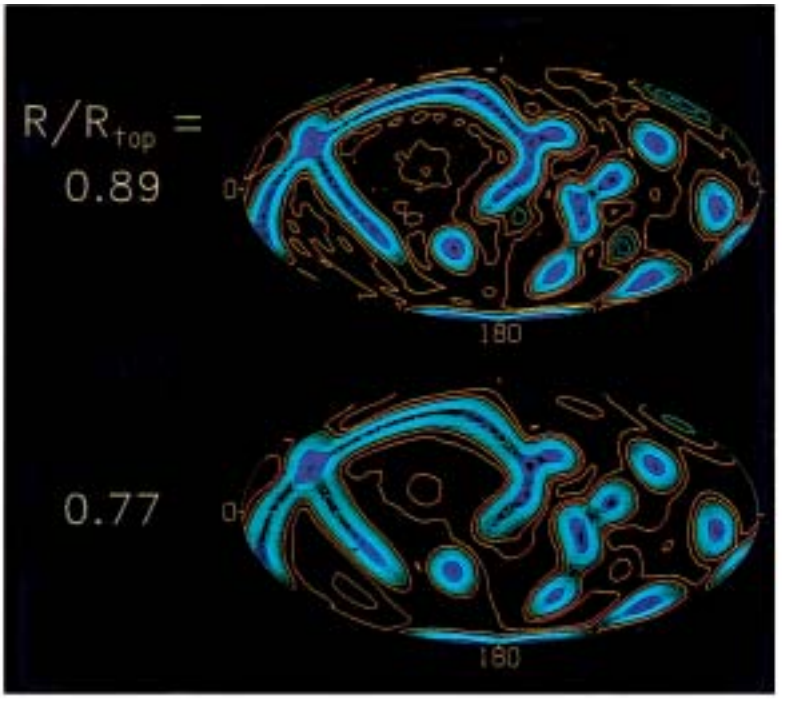

(a)

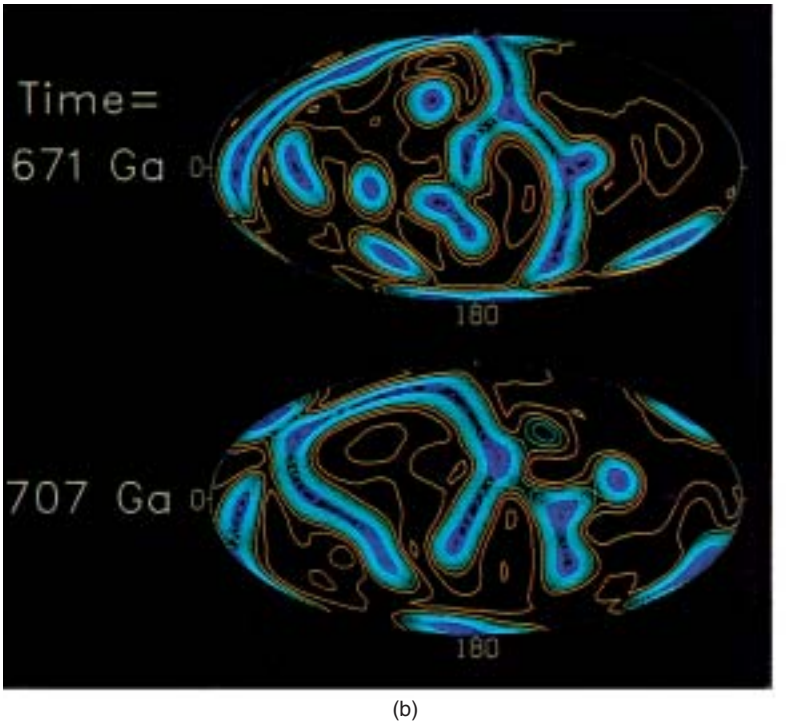

(b)

Figure 10.33. Contours of radial velocity in the calculation of Figure 10.32 for different depths at a given instant of time (a) and for different times midway through the shell (b). After Bercovici et al. (1989c).

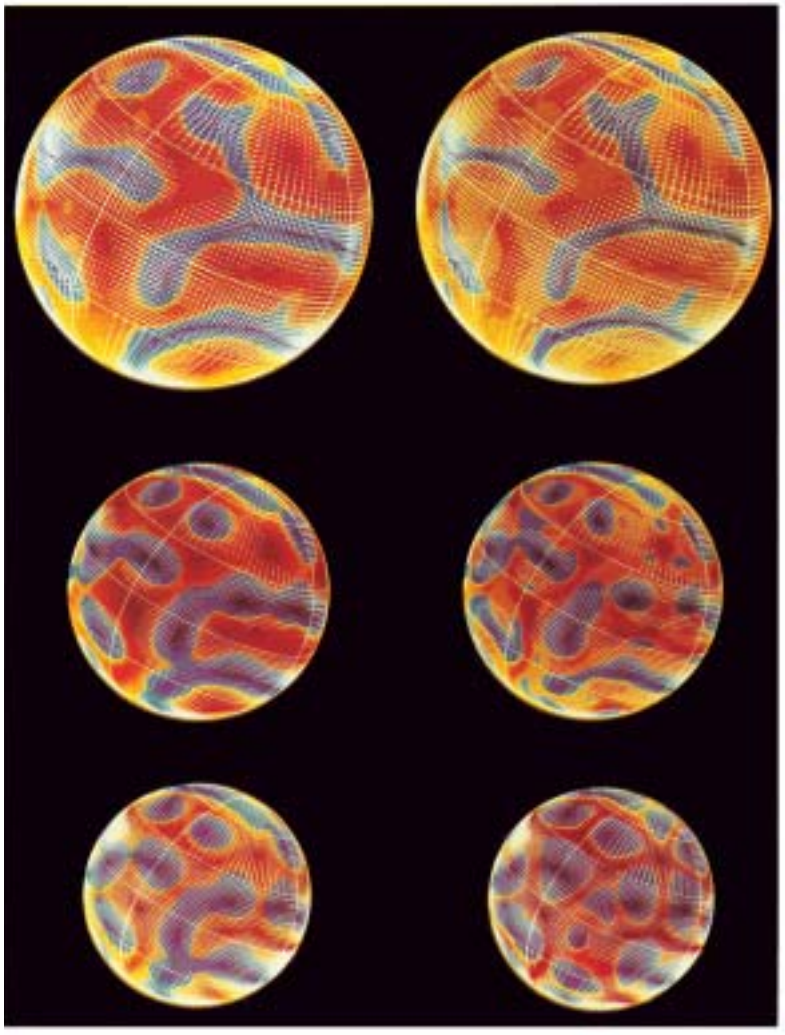

Figure 10.34. Convective velocities (left) and temperatures (right) at a single instant of time in three constant radius surfaces (5,940, 4,350, and 3,770 km) in a numerical model of fully three dimensional thermal convection in a spherical shell of compressible fluid with constant viscosity heated largely from within. The spherical surfaces are scaled according to their radii. The colors in the three plots on the left represent the radial component of velocity with a contour increment of 1.5 mm yr^{-1}. Reds and yellows represent upflow (maximum velocity 12 mm yr^{-1}). The colors on the right represent the temperature relative to the spherically averaged value at each radius with a contour increment of 50 K. Reds and yellows represent hot fluid (temperature anomaly maximum 400 K) and blues represent cold fluid (temperature anomaly minimum −650 K). The arrows represent the direction and amplitude of the horizontal velocity in these surfaces. All arrows are scaled in the same way (maximum velocity 20 mm yr^{-1}, velocities less than 2 mm $yr^{-1}$are not plotted). The top and bottom boundaries of the shell are isothermal and stress free. About 80% of the heat flow through the top surface is generated inside the shell whose inner and outer radii are 3,480 and 6,370 km. Parameters are identical to the case in Glatzmaier et al. (1990) (the uniform rate of internal heat generation is 10^{-11} W kg^{-1}, it is incorrectly given as 10^{-14} W kg^{-1} in Glatzmaier et al., 1990). In physical space the grid contains 33 radial levels (more densely packed near the boundaries), 96 latitudinal points, and 192 longitudinal points. In spectral space, spherical harmonics up to degree and order 63 are retained. The integration time step in the calculation is 10^6 yr. The Grüneisen parameter, specific heat at constant pressure, thermal conductivity, and dynamic viscosity are constant with values 1.1, 1.2 kJ K^{-1} kg^{-1}, 23 W K^{-1} m^{-1}, and 5.6×10^{22} Pa s. The adiabatic reference state is a polytrope with index 0.4, a zero-pressure bulk modulus of 115.15 GPa, a zero-pressure density of 3,500 kg m^{-3}, a density at the bottom of 5,570 kg m^{-3}, a temperature at the bottom of 3,000 K, and a temperature at the top of 1,800 K. The heat flux out of the top is about 5×10^{13} W. The volume-averaged Rayleigh number due to both the superadiabatic temperature drop and the internal heating is 1.6×10^6, about 200 times greater than the critical Rayleigh number required for the onset of convection. The bottom and top surfaces are held at 3,270 and, 1,070 K, respectively. After Glatzmaier et al. (1990).

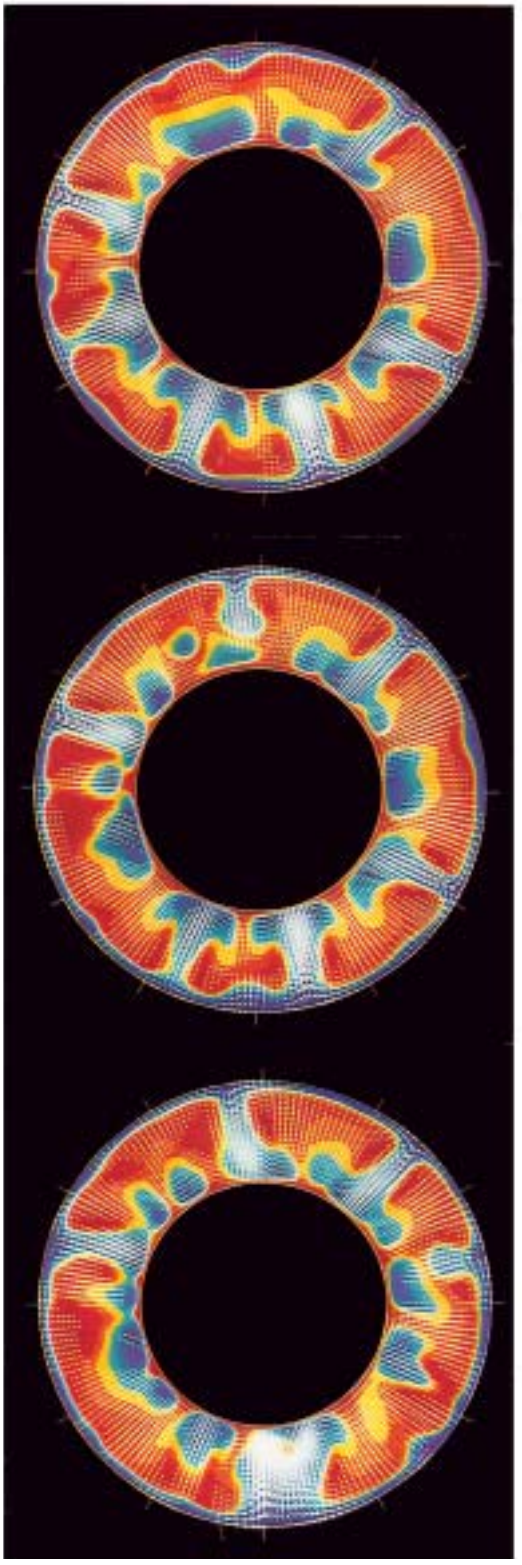

Figure 10.35. Equatorial cross-sections of convective velocities and thermal anomalies in the flow of Figure 10.34. Time increases from top to bottom (the time steps are at intervals of 200 Myr). The thermal anomalies are temperatures relative to the radially dependent adiabatic temperature profile with a contour increment of 50 K. Reds and yellows represent hot fluid (maximum 300 K) and blues represent cold fluid (minimum of −750 K). The arrows represent velocities in the cross-sectional plane and are scaled as in Figure 10.34. After Glatzmaier et al. (1990).

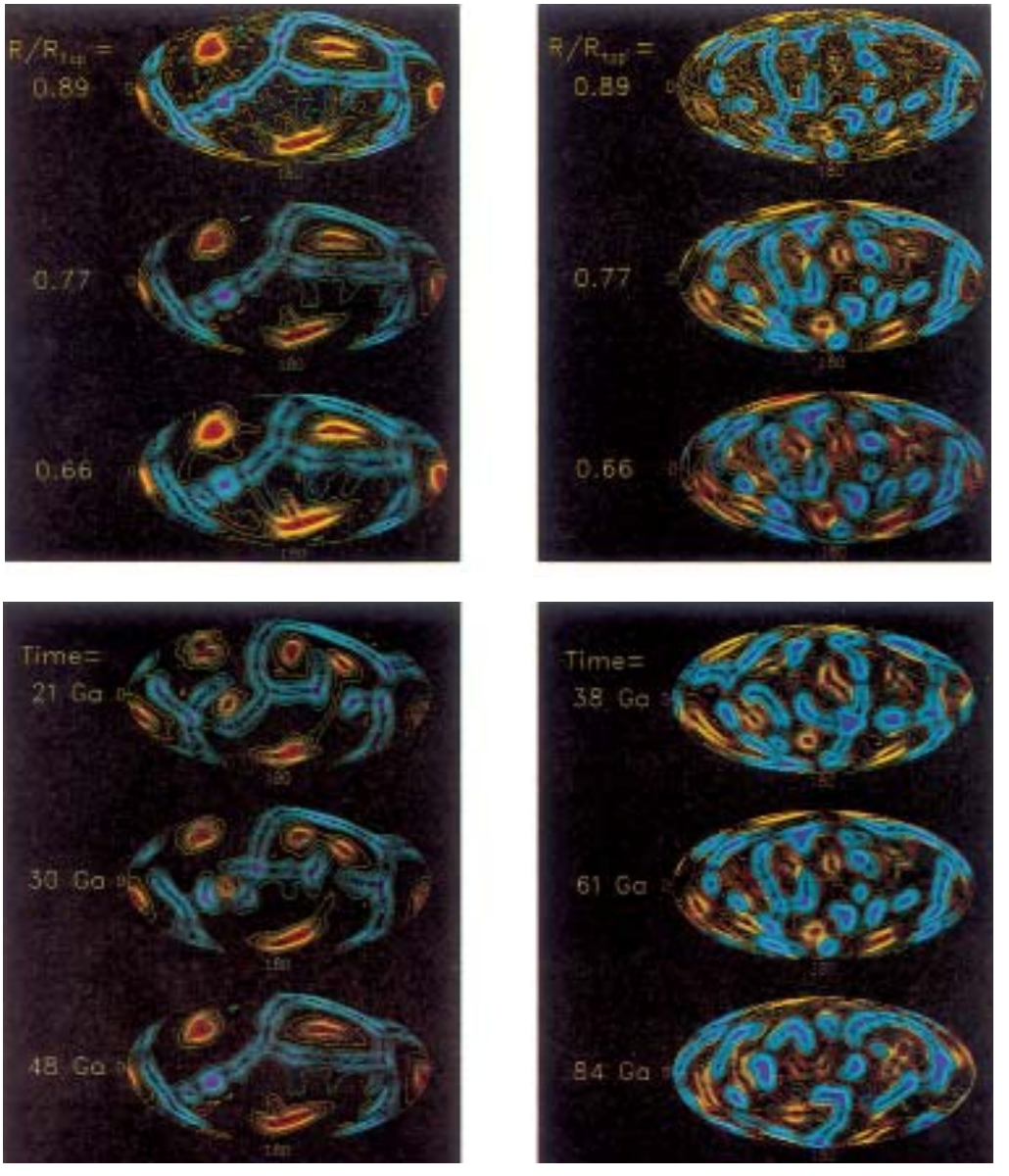

Figure 10.37. Styles of three-dimensional convection in a spherical shell of compressible fluid heated both from within and from below. The planforms on the left are for 50% internal heating, while those on the right are for 80% internal heating. The panels show radial velocity contours on an equal-area projection of a spherical surface at different depths for one time (top) and at different times for one depth ($r/r_{\text{top}} = 0.77$) (bottom). Colors represent equal intervals of velocity (reds and yellows are upflows, blues are downflows). The Rayleigh numbers in both cases are about 100 times the critical *Ra* for the onset of convection. After Bercovici et al. (1989c).

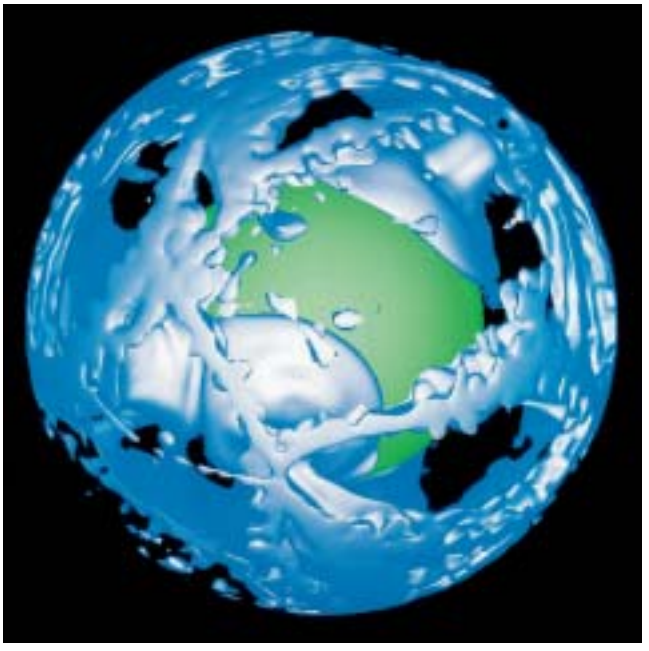

Figure 10.38. A snapshot of a cold isothermal surface in the model of Tackley et al. (1993). The blue surface is 110 K lower in temperature than the horizontally averaged temperature at every radius. The green surface is the lower boundary of the model (the core). A network of interconnected linear downflows is visible in the upper mantle with three large cylindrical downwellings in the lower mantle that spread out into pools of cold material above the core–mantle boundary.

Figure 10.39. A hot isothermal surface in the model of Tackley et al. (1993) at the same instant of time as in Figure 10.38. The red surface shows where the temperature is 110 K higher than the reference state adiabat at all depths. A single plume from the core–mantle boundary supplies hot material to a region of the upper mantle. Most broad hot regions of the upper mantle are not directly linked to lower mantle structures.

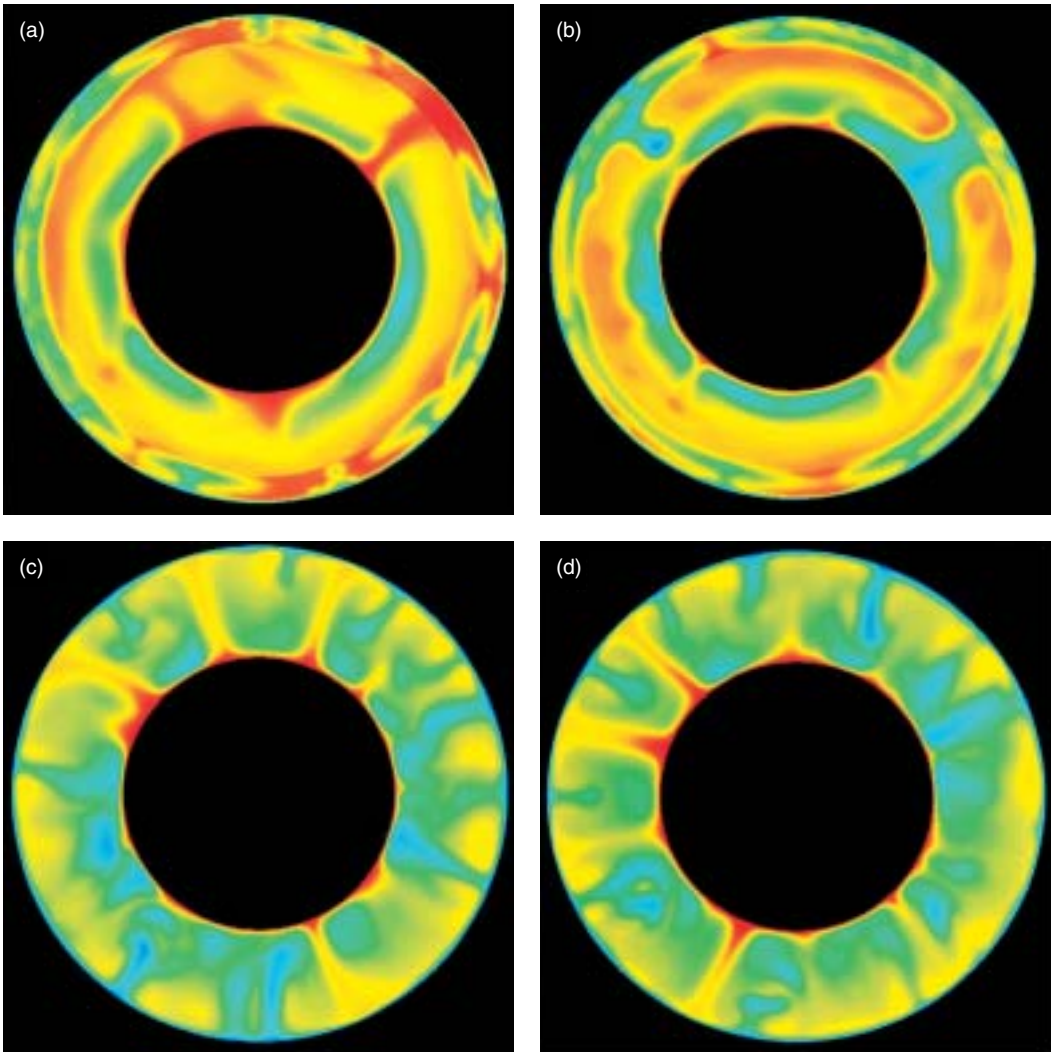

Figure 10.40. Different cross-sectional slices of the superadiabatic temperature field in the model of Tackley et al. (1993) at the same time as in Figures 10.38 and 10.39 (a) and (b). Red is hot and blue is cold with the temperature scale varying between +350 K and −1,050 K. (c) and (d) show similar cross-sections of superadiabatic temperature for a numerical calculation that does not include the endothermic phase change (Tackley et al., 1993). The temperature scale in (c) and (d) ranges between +220 K and −780 K.

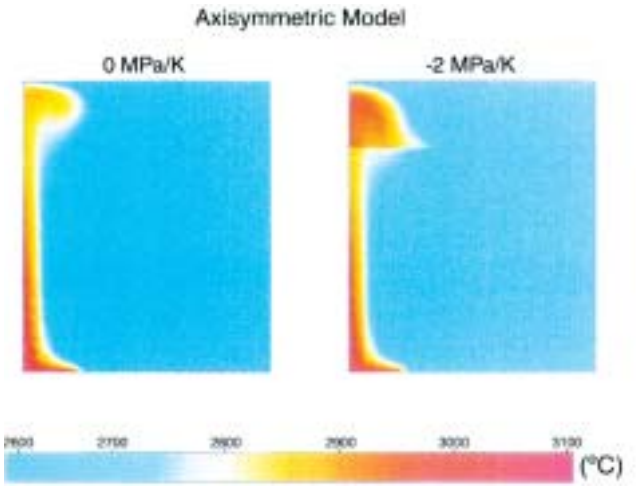

Figure 10.41. Temperature fields of two axisymmetric plumes, one that has passed through an endothermic phase change (right) and one that has not (left).The plume that went through the phase change is about 100 K hotter than the other plume. After Schubert et al. (1995).

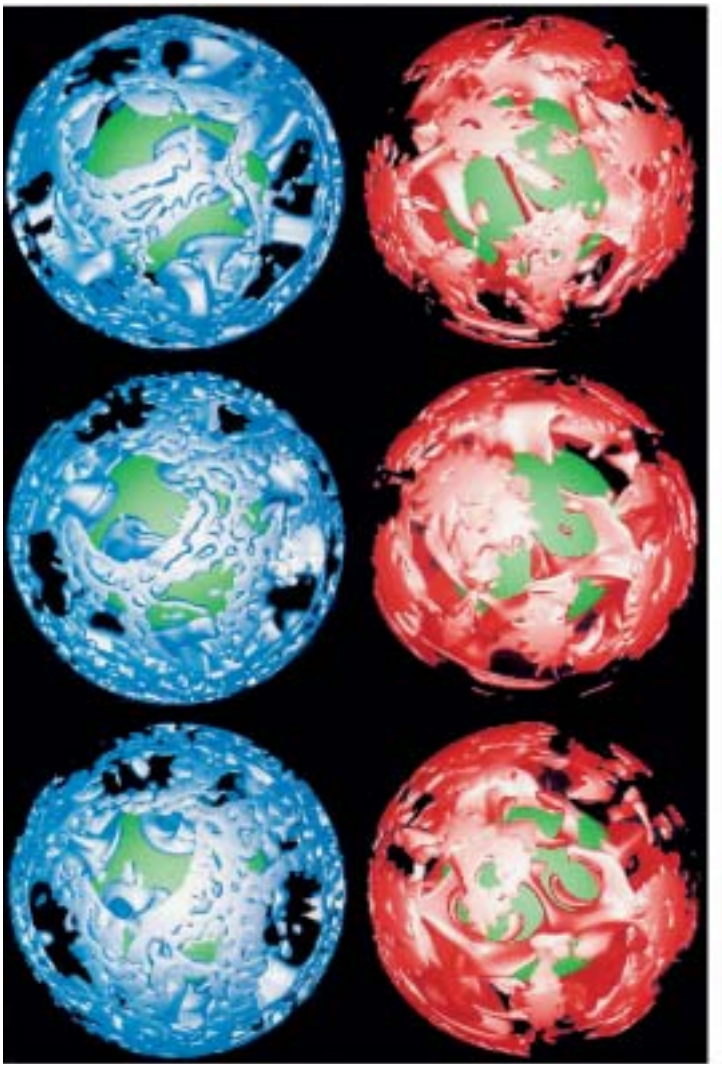

Figure 10.43. Cold downflows (left) and hot upflows at three times (at intervals of about 500 Myr) during the simulation of mantle convection by a model containing phase transitions at depths of 400 km and 670 km (Tackley et al., 1994). Cold and hot isosurfaces show where the temperature is 110 K lower and higher, respectively, than the horizontal average. The core–mantle boundary is shown in green. Time increases down the figure.

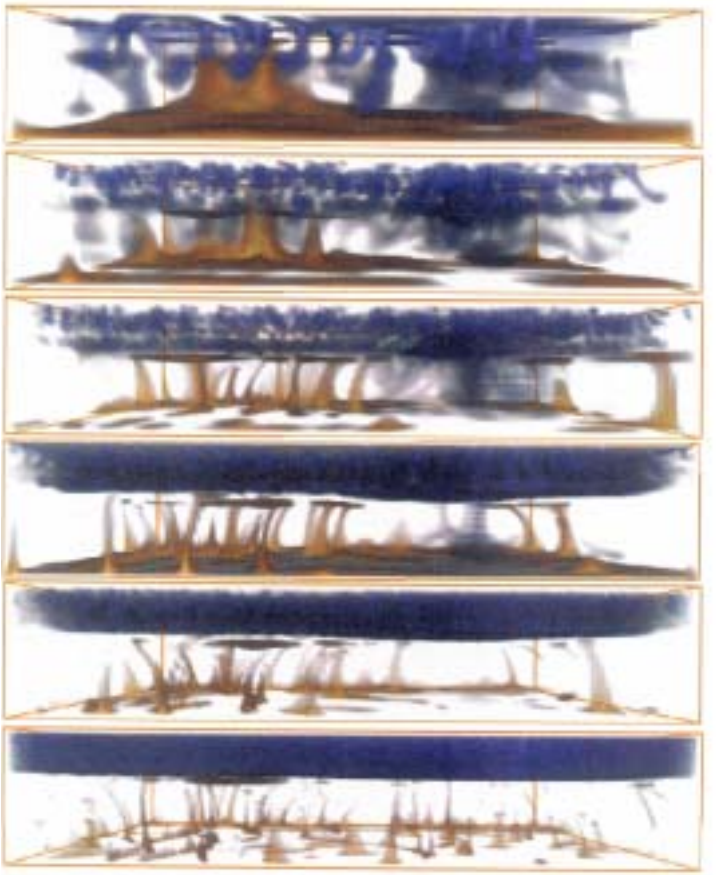

Figure 10.45. Simulations of three-dimensional convection with an endothermic phase change at different values of the Rayleigh number (*Ra* increases downward). At lower values of *Ra* the phase change does not significantly influence the whole-layer flow (top). At intermediate values of *Ra* (middle) partially layered, avalanche-modulated convection occurs. At the highest values of *Ra* (bottom) the phase change completely layers the flow and there are no mantle avalanches. After Yuen et al. (1994).

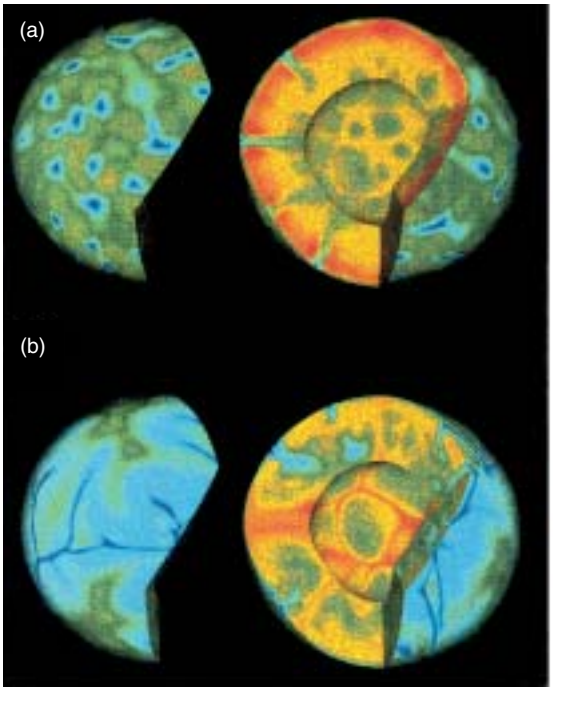

Figure 10.46. Temperature distribution in a model of internally heated convection with (a) constant viscosity and (b) lower mantle viscosity = 30 times upper mantle viscosity. The upper surface of the figure is 250 km below the isothermal surface of the model. Red is hot, blue is cold. After Bunge et al. (1996).

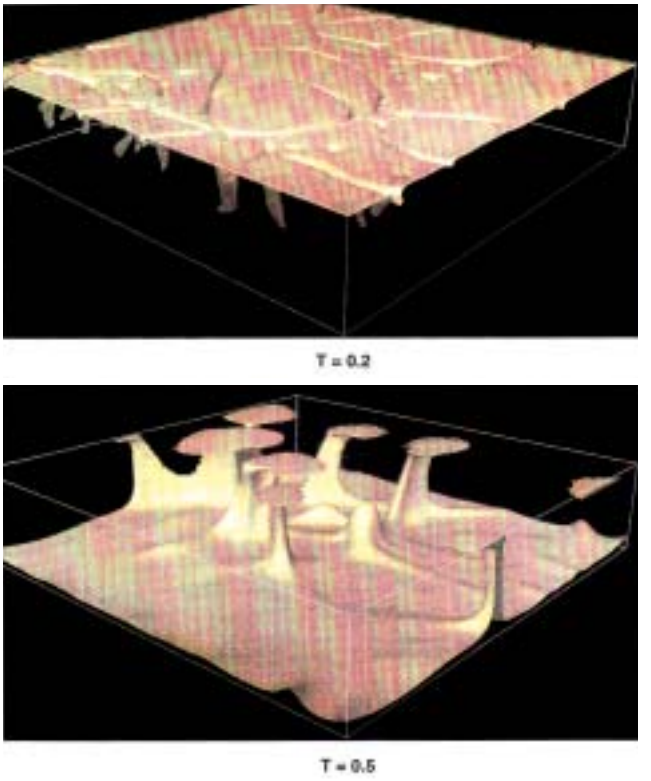

Figure 10.53. Isosurfaces of dimensionless temperature at a surface Rayleigh number of 5×10^6 in the three-dimensional compressible convection model of Balachandar et al. (1992, 1993). The $T = 0.2$ isosurface shows the descending sheets while the $T = 0.5$ isosurface reveals the upwelling cylindrical plumes.

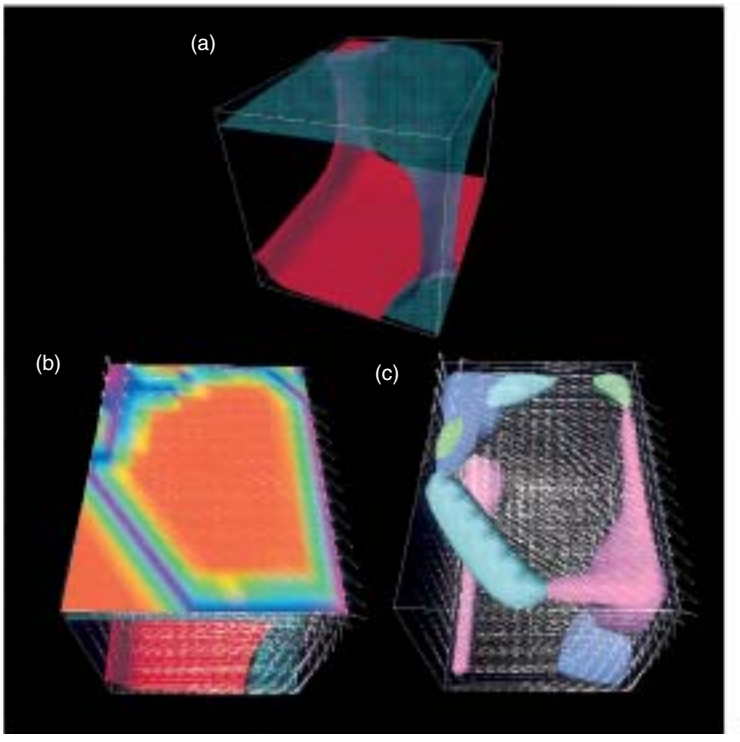

Figure 10.59. Model results for velocity, viscosity, horizontal divergence, and vorticity driven by a prescribed thermal buoyancy field in a rectangular box containing a high-viscosity lithosphere with strain rate weakening viscosity overlying an isoviscous mantle with Newtonian rheology. (a) Temperature isosurfaces (red is hot, blue is cold), (b) viscosity (orange is large, violet is small, viscosity varies between 10^{-1} and 10^4 times the mantle viscosity) and velocity vectors, and (c) horizontal divergence/convergence (light and dark purple) and vertical vorticity (green and blue). After Tackley (1998a).

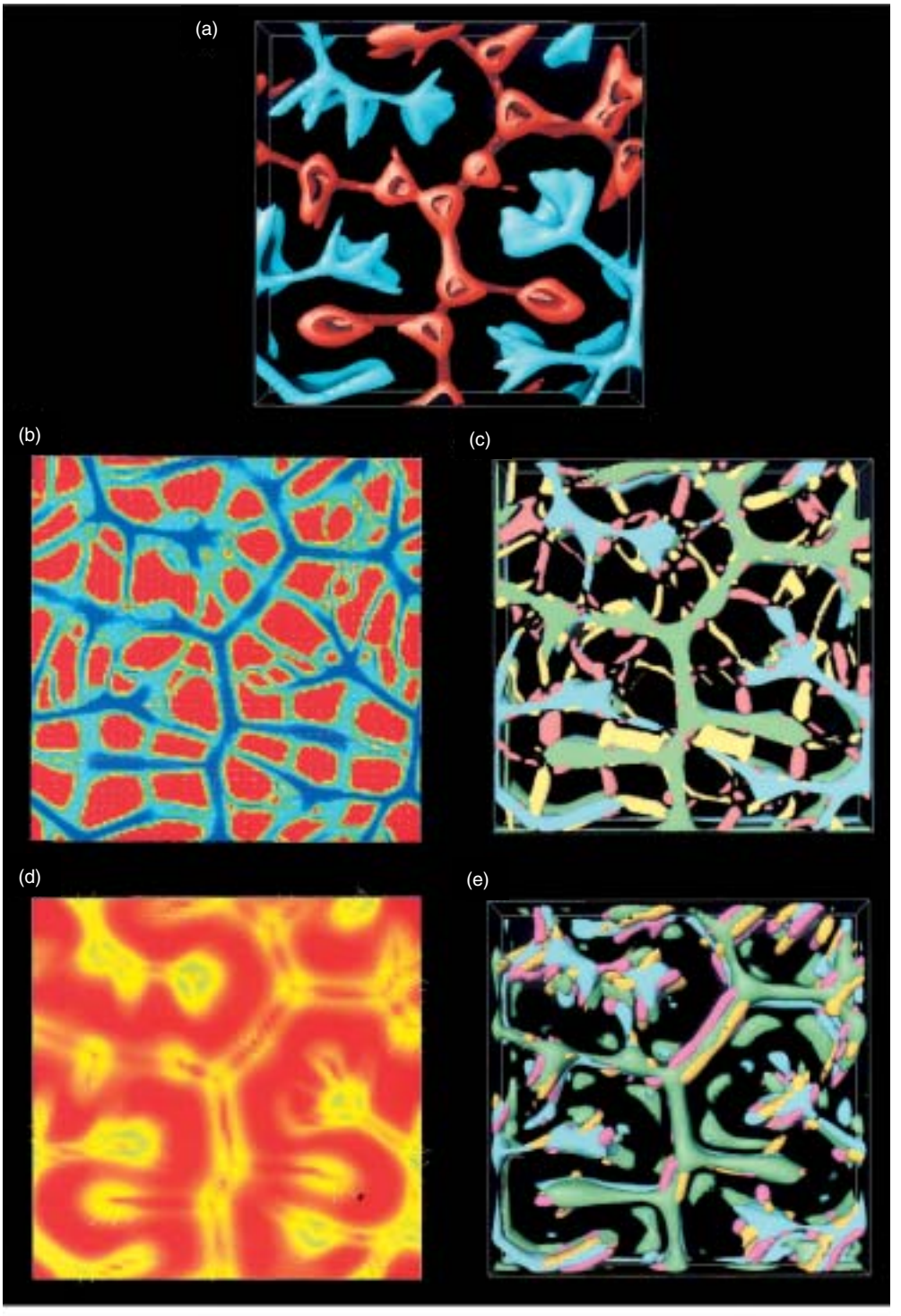

Figure 10.60. Similar to Figure 10.59 for a wide box of dimension $8 \times 8 \times 1$. The panels in (d) and (e) are similar to (b) and (c) but for a viscoplastic rheology. After Tackley (1998a).

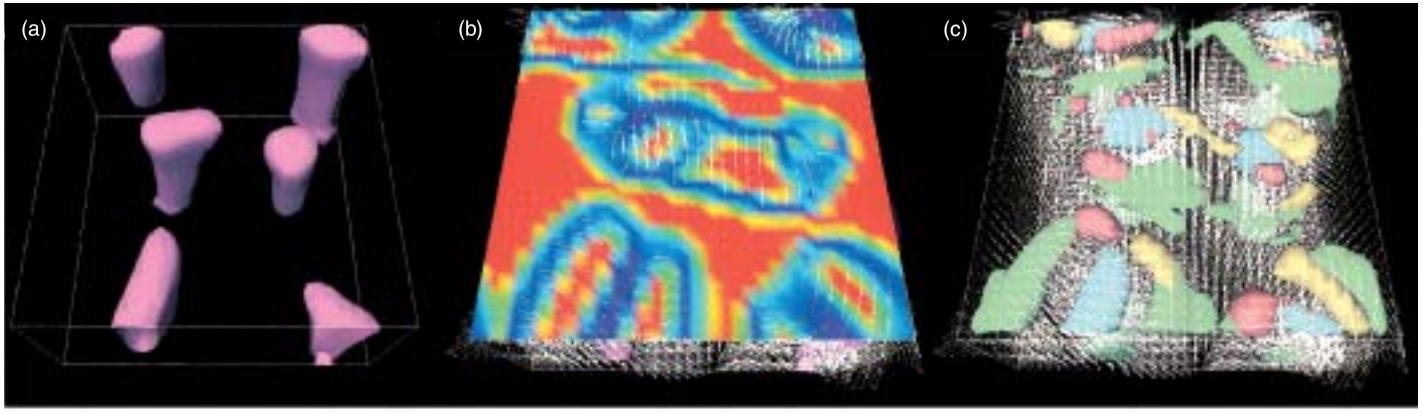

Figure 10.61. Similar to Figure 10.59 for flow driven by thermal buoyancy forces from a convection calculation with only internal heating. The residual temperature isosurface in (a) shows the pattern of downwelling – mainly cylindrical, but sometimes elongated (lower left). (b) Velocity vectors and lithospheric viscosity. (c) Horizontal divergence (green and blue) and vertical vorticity (yellow and mauve). After Tackley (1998a).

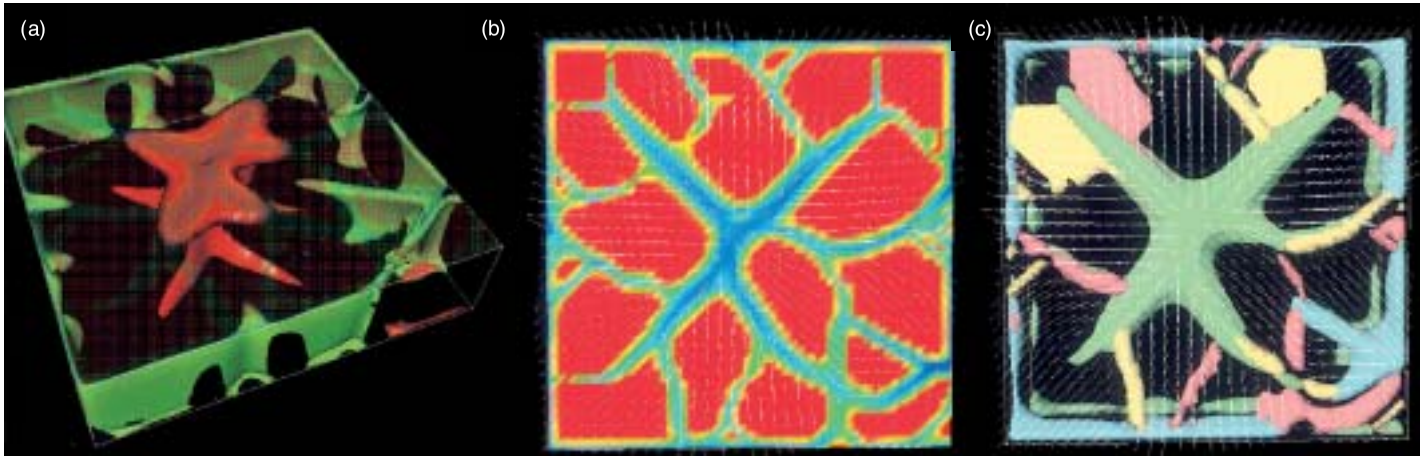

Figure 10.62. Similar to Figure 10.59 for a compressible, Earth-like, basally heated model in a $4 \times 4 \times 1$ box. After Tackley (1998a).

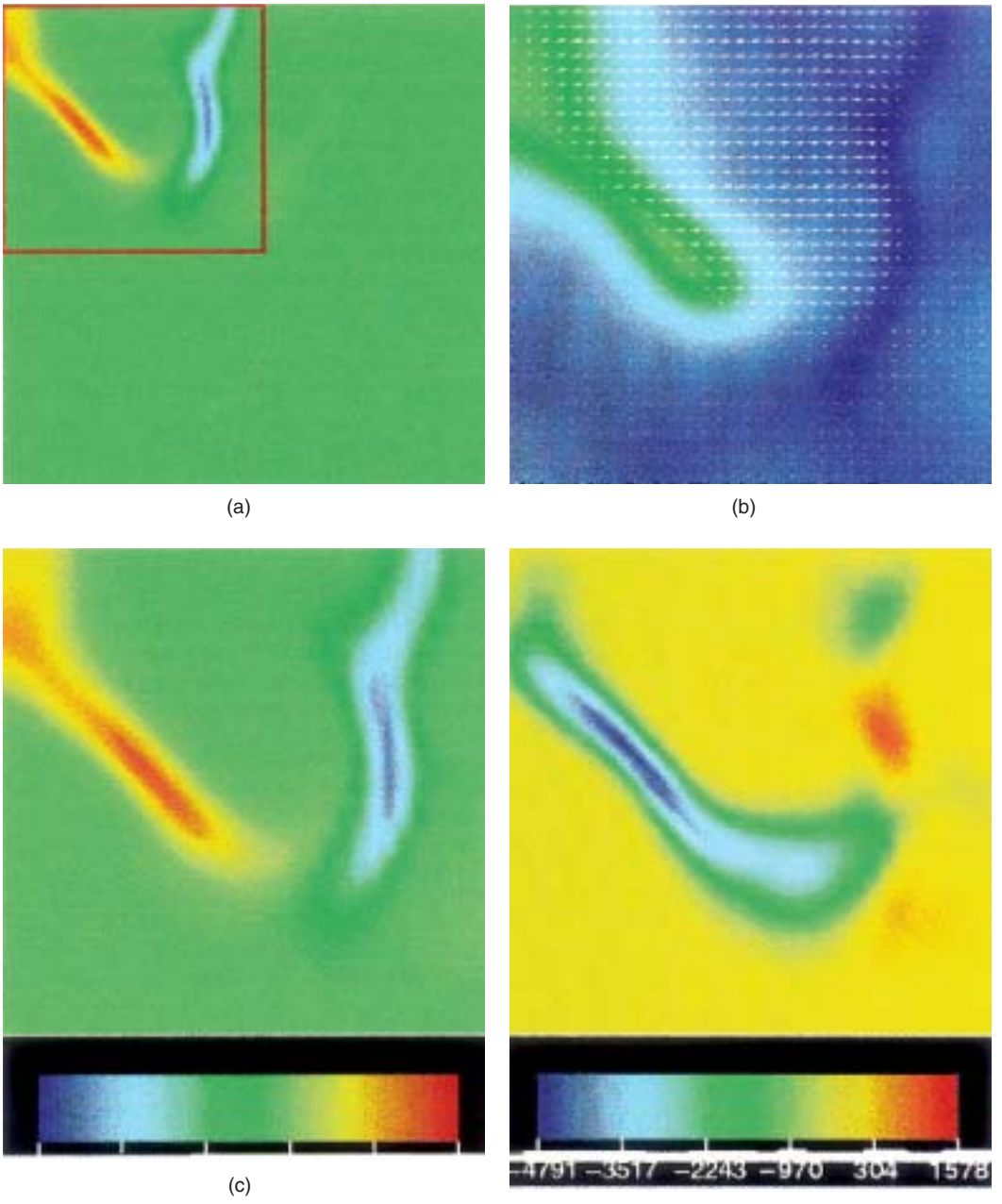

Figure 10.63. Plate-like behavior in the mantle convection model of Trompert and Hansen (1998). (a) Horizontal divergence (red) and convergence (blue). The entire top surface of the box is shown. Narrow zones of divergence and convergence are shown in the upper left corner. The red square outlines the region shown in more detail in (b), (c), and (d). (b) Velocity vectors and the temperature field slightly below the surface (blue is cold and green is warm). (c) Horizontal divergence. (d) Vertical vorticity.